




3D Time-Lapse Electrical Resistivity Imaging of Rock Damage Patterns and Gas Flow Paths Resulting from Two Underground Chemical Explosions

TIM C. JOHNSON,¹  H. A. KNOX,^{1,2} C. STRICKLAND,¹ C. JOHNSON,¹ J. LOWREY,¹ D.P. SPRINKLE,¹ D. LINNEMAN,¹ V. VERMEUL,¹ E. ROBEY,² K. CHOJNICKI,^{1,2} M. INGRAHAM,² J. FELDMAN,^{1,2} and H. MILEY¹

Abstract—Rock damage from underground nuclear explosions (UNEs) has a strong influence on sub-surface gas movement and on seismic waveform characteristics, both of which are used to detect UNEs. Although advanced numerical simulation capabilities exist to predict rock damage patterns and corresponding detection signals, those predictions are dependent on (generally) unknown properties of the host rock. For example, the effects of in-situ mechanical heterogeneities on the explosively generated damage/fractures that provide gas flow pathways to the surface are not well understood, due largely to the difficulty in accessing and characterizing the near-source region. In this paper we demonstrate the emerging use of electrical resistivity tomography (ERT) for imaging rock damage and gas flow patterns resulting from two relatively small-scale underground chemical explosions. Pre-explosion ERT and crosshole seismic imaging revealed a natural fracture zone within the test bed. Post-explosion imaging revealed that the damage zone was non-symmetric and was focused primarily within the pre-existing fracture zone, located 10 m above the first explosion and 5 m above the second explosion. Time-lapse ERT imaging of heated air injected into the detonation borehole revealed the primary gas flow paths to be within the upper margin of the same primary damage zone. These results point to the utility of ERT imaging for understanding rock damage and gas flow patterns under experimental conditions, and to the importance of understanding the effects of geologic heterogeneity on UNE detection signals, particularly gas surface breakthrough times.

Keywords: Resistivity, Imaging, Underground explosion, Rock damage.

1. Introduction

Seismic monitoring and environmental radionuclide monitoring are two primary methods of detecting the occurrence of underground nuclear

explosions (UNEs). Seismic energy recorded at monitoring stations contains information concerning the timing, location, and magnitude of an underground explosion (e.g. Denny & Johnson, 1991; Ekström & Richards, 1994; Ford & Walter, 2010). In addition, seismic waveforms implicitly contain further information concerning the geologic structure along the travel paths, which is vitally important at local and regional distance scales. Although seismic monitoring is the primary method for detecting and locating underground explosions, current understanding does not enable discrimination between nuclear and chemical explosions. Atmospheric radionuclide monitoring, which relies on the detection of radioactive gases and particulates that migrate from the UNE working point to the surface and are subsequently transported through the atmosphere, is currently the primary method of nuclear versus non-nuclear discrimination (e.g. Bowyer et al., 1997, 2002; Kalinowski et al., 2010; Lowrey et al., 2013).

The importance of the first few hundred meters of signal propagation of both waveform and materials could be amplified when considering lower yield nuclear tests because the signatures are lower in magnitude and may suffer from severe distortion in the local to regional scales of the subsurface. One key question is how the near field (~ 0 to 200 m from the working point) geologic response to the explosion influences far field signals. Of particular interest are how rock damage patterns, such as rock crushing, block motion, spallation, and fracturing, influence gas flow to the surface and far-field seismic characteristics such as the generation of S-waves (e.g. Snelson et al., 2013; Stroujkova, 2018). Although advanced

¹ Pacific Northwest National Laboratory, Richland, WA, USA. E-mail: tj@pnnl.gov

² Sandia National Laboratories, Albuquerque, NM, USA.

hydrodynamic modeling capabilities exist, data to validate or otherwise inform simulation codes are sparse, primarily due to sampling requirements imposed by subsurface heterogeneity and the general difficulty of accessing the near-source region.

In this paper we demonstrate an emerging capability for imaging rock damage patterns and gas flow paths from underground explosions using time-lapse 3D, i.e. 4D, electrical resistivity tomography (ERT). ERT is an established method of remotely imaging the bulk electrical conductivity (BEC, the reciprocal of resistivity) of the subsurface. The underlying premise is that rock damage modifies rock porosity, saturation and electrical current flowpaths and therefore alters BEC. The corresponding change in BEC with respect to pre-explosion conditions is imaged using time-lapse ERT, thereby illuminating the damage zone. To image gas flow paths, we inject heated air into the post-explosion source point. As gas flows from the source point through the fracture zones, it evaporates water and decreases BEC. The decrease in BEC from pre-injection conditions imaged via time-lapse ERT illuminates the primary post-explosion gas flow paths.

We demonstrate ERT-based damage imaging for two relatively small underground chemical explosions in a mesoscale (~ 16 m in diameter and 70 m deep) testbed composed of a massive, dense rhyolite. The source packages were designed to have different gas generation and detonation velocity characteristics, but with an equivalent total yield of 5 kg TNT each. In each case, the damage zone was significantly influenced by pre-existing heterogeneity within the testbed, which was identified by ERT and crosshole seismic velocity imaging. Namely, primary damage patterns were focused within a pre-existing fracture zone rather than being focused around the working point. Gas flow imaging revealed that primary gas flowpaths occurred within the same damage zone. These results provide novel evidence regarding how geologic heterogeneity influences rock damage patterns and corresponding gas flow paths, and that the scale of relevant heterogeneity is smaller for lower yields.

ERT imaging for damage assessment was conducted under saturated conditions for the experiments presented in this paper. We conclude with evidence

and comments regarding the anticipated applicability of ERT for assessing explosion-induced damage under partially saturated conditions.

2. Materials and Methods

2.1. Blue Canyon Dome Testbed

The testbed is situated within the Blue Canyon Dome at the Energetic Materials Research and Testing Center (EMRTC) located west of Socorro NM, USA. The dome itself, at least in relevance to the testbed, is comprised of two geologic units: a fanglomerate that infilled a graben structure after the formation of the dome and the rhyolite below it. The rhyolite, which has been directly sampled down to 122 m, has compressive strengths of nearly 234 MPa (Bauer, 2021). The rhyolite exhibits some flow banding and minimal fractures but is otherwise massive in nature with low primary permeability. Socorro Mountain, the ancient Caldera that Blue Canyon Dome sits on, was part of the Mogollon-Datil Volcanic Field. Regionally, Socorro Mountain lies at the edge of the Rio Grande Rift, putting it on the margins of an extensional regime. The water table is at least 100 m below the testbed and had no effect on the testing.

2.2. Characterization and Monitoring Array

Figure 1 shows plan and cross section views of monitoring boreholes and associated instrumentation that surround the ground zero (GZ) borehole, which is where the explosive packages were detonated. The GZ borehole was cased with 20 cm (8 in.) steel casing to approximately 25 m below ground surface and sealed at the surface with a Class 1500 Bolted Flange Tree with gusset straps welded to the casing. GZ was left uncased from 25 m to its terminating depth of approximately 78 m. The top of the flange was removed between explosive experiments to provide access to the GZ borehole. Each of the eight monitoring boreholes were 20 cm (8 in.) in diameter and completed with a 10 cm (4 in.) PVC casing. The annulus of each monitoring borehole (i.e., the volume between the PVC casing and the borehole wall) was

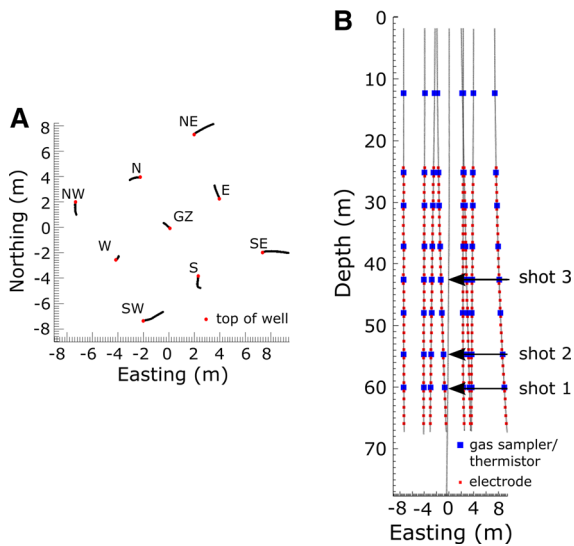


Figure 1

A Plan view of Blue Canyon Dome monitoring boreholes. Explosive packages were placed in the ground zero (GZ) borehole. The remaining boreholes house monitoring instrumentation. Red dots show the top of the borehole and black lines show the borehole deviation with depth. **B** Cross section view of Blue Canyon Dome. Red dots show ERT electrode locations (32 per borehole). Blue dots show gas sampling and thermistor locations (8) per borehole. Explosions 1 and 2 were located at 60 m and 55 m below ground surface respectively

instrumented with 32 stainless steel mesh electrodes, 8 gas sampling ports with thermistors, and distributed temperature sensing (DTS) fiber.

Each gas sampling port was encased in a well-sorted 30 cm (12 in.) sand lift to enable gas to flow freely from the formation to the port, sealed above and below with a 10–15 cm (6–8 in.) lift of epoxy. Between gas sampling intervals, the annulus was filled with an electrically resistive cement grout designed to discourage current flow through the annulus during ERT measurements. Combined, the eight monitoring boreholes provided the capability to conduct cross-hole ERT imaging, gas sampling, and temperature monitoring through instrumentation sealed in each borehole annulus. The casing was left open for other sensing and imaging modes including cross-hole seismic velocity tomography, which was used for baseline characterization of the testbed as discussed below. Figure 2A shows a photograph of a monitoring borehole and instrumentation being installed in the annulus of a monitoring well during

construction. Figure 2B shows a photograph of the GZ wellhead.

2.3. Explosion Sequence

Explosive Experiments 1 and 2 were detonated in the GZ borehole at depths of 60 m and 55 m below ground surface, respectively. Each explosive was placed in a canister and suspend from the wellhead. To compare the effects of gas generation and detonation velocity on damage patterns and seismic responses, each experiment used a different explosive composition. Explosive 1 was comprised of nitromethane which had a higher detonation velocity (6100 m/s) and lower gas generation with respect to Explosive 2. Explosive 2, ammonal, has a slower detonation velocity (3600 m/s) tailored by changing the aluminum to the ammonium nitrate base ratios) and a higher gas production. Experiments 1 and 2 were separated in time by over 10 months, which allowed the subsurface to return to a steady state condition after Experiment 1.

As a safety measure, the GZ borehole was filled with water prior to each detonation to eliminate potential water-hammer effects on the wellhead that might result from a partially filled borehole. As described below, this caused fractures connected to GZ to fill with water which provided a saturated baseline for the time lapse ERT imaging. Once a baseline ERT survey was collected (requiring approximately 35 min) the explosive package was lowered to position and detonated. Upon detonation, high pressure water ejected from a small (~ 1 cm diameter) pressure relief hole in the wellhead for up to 5 min.

The general sequence of events from detonation to a relative steady state condition within the testbed were as follows:

1. At detonation, a shockwave moves from the working point outward into the formation. In the near-wellbore environment, this shockwave pulverizes and fractures the borehole, as is evidenced in the camera footage of the ground zero borehole.
2. A high-pressure pulse develops in GZ due to the production of gas from the explosive reaction and interaction with the water-filled borehole. Pressure

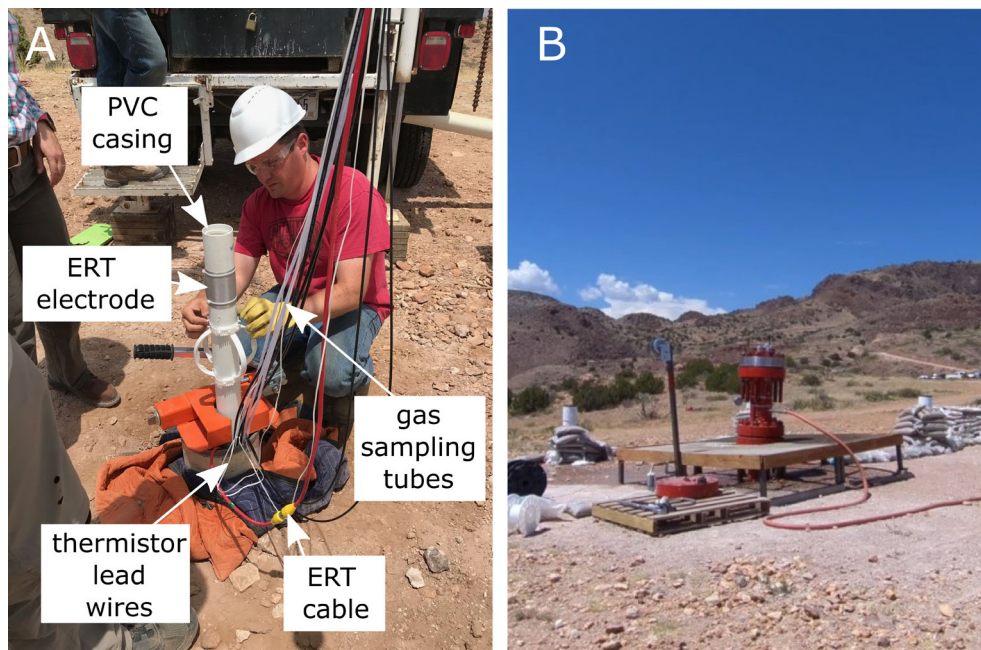


Figure 2

A Photograph of a monitoring borehole and components during construction. **B** Photograph of the ground-zero wellbore wellhead

observed at the wellhead exceeds 193 MPa (the upper limit on the pressure sensor).

3. Explosively generated gas and water from the borehole are driven into the surrounding rock and out of the pressure relief hole on the wellhead. During late times (10 s of minutes) we have observed degassing of the borehole as gas bubbles rise through the remaining water column.
4. GZ pressure dissipates over several minutes to atmospheric pressure. Water that was not ejected from the wellhead forms a residual pool at some level in GZ that drops as the formation drains.
5. Formation water drains back into GZ and/or downward through other flow pathways within the rock matrix. This dynamic process usually results in some migration of water back into GZ and then also out of the testbed via larger interconnected natural and explosively generated fractures. Before explosive Experiment 1, it was observed that the borehole was not water-tight and was connected to a pre-existing fracture that allowed the borehole to drain significantly (i.e., complete drainage occurred over hours). As described below, the primary drainage pathway

was identified using crosshole seismic velocity and time-lapse ERT imaging.

6. Water continues to drain from the testbed until a pseudo-steady state of saturation is reached.

2.4. Heated Air Injection Test

After the testbed recovered from explosive Experiment 2 and reached a relative steady state condition (approximately two weeks of draining/drying), a heated air injection test was conducted to assess primary gas flow pathways from GZ into the formation and onward through the testbed. Gas flow was injected at 70 °C and 2500 L/min for approximately 10 days. Flow pathways were identified through pressure monitoring at the gas ports and through time-lapse 3D ERT imaging. Temperature was also recorded at each gas port but no changes in temperature were registered over the duration of the injection.

Heated air flow causes a change in BEC that can be imaged with time-lapse ERT through two mechanisms. First, rhyolite behaves as a semiconductor in

terms of the relationship between temperature and BEC. Namely, BEC increases with temperature. As the heated air moves through the testbed it may heat the surrounding rhyolite, causing an increase in BEC along the air flow pathways. Second, as relatively dry, hot air moves through the testbed it evaporates water causing a decrease in saturation (and air temperature) and thus a decrease in BEC along the primary flow paths. The effects of increasing temperature and decreasing saturation have opposing effects on BEC. However, as will be shown, the effects of evaporation and decreasing saturation dominated the BEC response such that primary gas flowpaths were identifiable as decreases in BEC from pre-injection conditions.

2.5. Crosshole Seismic Velocity Tomography

Crosshole seismic velocity tomography is a method of imaging the seismic velocity structure of the subsurface, which can be used to infer mechanical properties of the testbed (e.g., Angioni et al., 2003; ASTM, 2007; Dietrich & Tronicke, 2009; Luna & Jodi, 2000). For example, unfractured and intact rhyolite is expected to exhibit greater seismic velocity than fractured or damaged rhyolite. Therefore, regions of decreased velocity may be diagnostic of fracture zones within the test bed.

Prior to explosive Experiment 1, 2D crosshole seismic velocity tomography data were collected between boreholes NE-SW (Fig. 1A). Crosshole seismic data were collected by filling the PVC casing with water (to enable seismic source coupling into the formation) generating a seismic pulse every 1 m within the source borehole SE, and recording the corresponding P-wave arrival times every 0.25 m within the receiving borehole NW. The seismic source was a P-wave Geotomographic Sparker powered by an IPG5000 and the receivers were hydrophones recorded on a Geometrics Geode Exploration Seismograph. To process the data, source-receiver geometry and corresponding P-wave travel times were used within a tomographic inversion algorithm to estimate the P-wave velocity distribution in each plane.

2.6. ERT Imaging

ERT is a method of imaging the direct-current (or low frequency) BEC of the subsurface using an array of electrodes (Singha et al., 2015). During a single ERT measurement, a voltage is applied across two electrodes (the current electrodes), causing current to flow through the subsurface from the positive to the negative current electrode. The corresponding potential generated in the subsurface is measured between two different electrodes (the potential electrodes). The basic datum of an ERT measurement is the observed potential normalized by the injected current, which has units of ohms and is often referred to as the transfer resistance. Many such four-electrode measurements, strategically collected to optimize imaging resolution, form an ensemble of measurements called a survey. In static imaging mode, single-survey data are tomographically inverted to produce an estimate (or image) of the BEC structure that gave rise to the measurements. In time-lapse imaging mode, identical surveys collected over time are inverted to estimate transient changes in BEC structure from some baseline state. Time-lapse difference imaging is particularly useful because the static effects of geology are removed from the image, revealing only what has changed over time (e.g., changes in BEC from rock damage or gas flow). ERT data were processed using the open source E4D code (<https://e4d.pnnl.gov>). Further details concerning the time-lapse imaging may be found in Johnson et al. (2010) and Singha et al. (2015).

2.7. Relationship Between BEC, Gas Phase Permeability, and Rock Damage

BEC quantifies the ease at which electrical current flows through the subsurface in the presence of an electrical potential gradient (i.e., an electric field). Analogously, gas phase permeability quantifies the ease at which gas migrates through the subsurface in the presence of a gas pressure gradient. Figure 3 shows a basic conceptual diagram illustrating how changes in BEC resulting from an underground explosion are diagnostic of rock damage and changes in gas phase permeability, for both saturated and unsaturated systems. We assume that the mineral

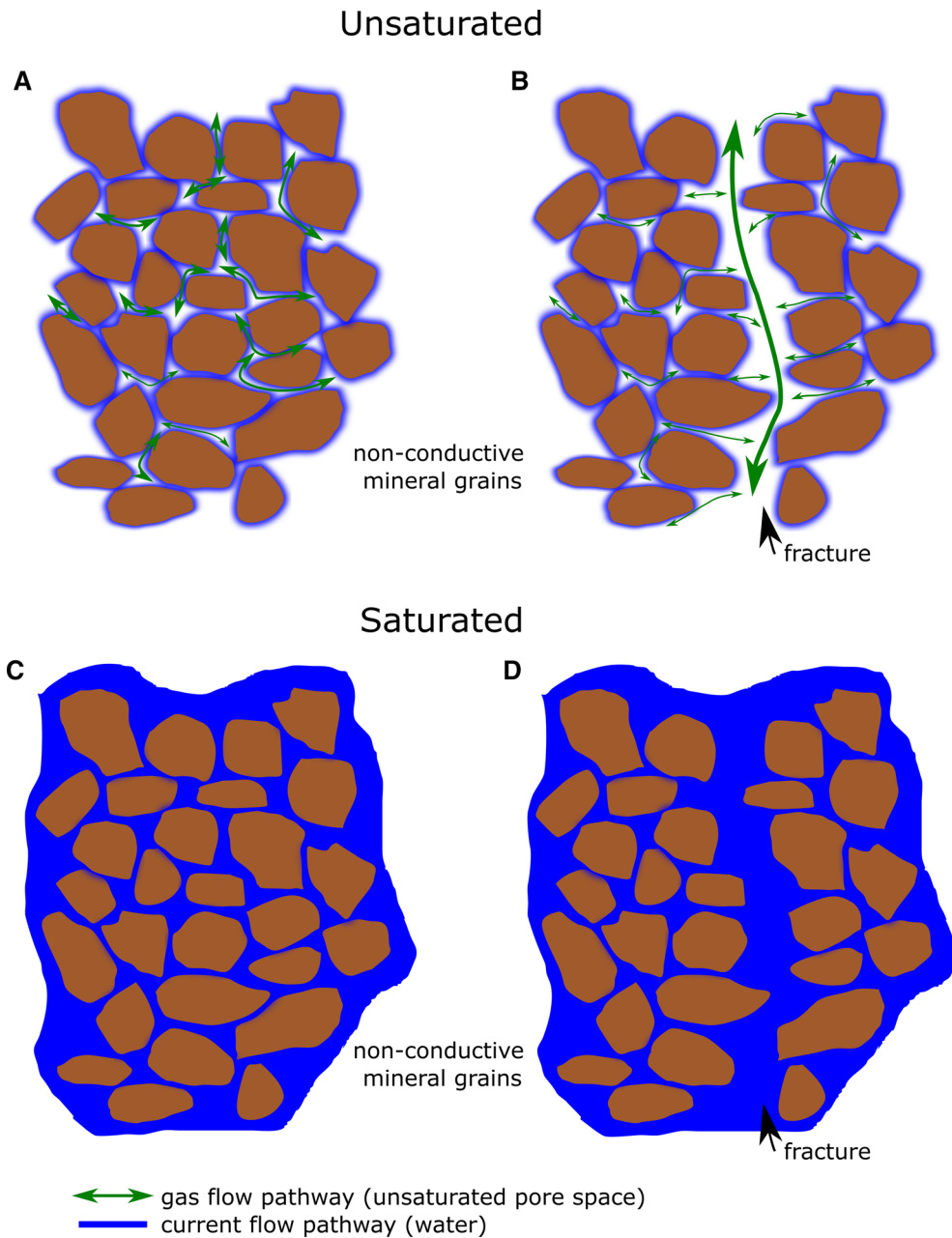


Figure 3

Basic conceptual diagram of current and gas flow pathways under unsaturated and saturated conditions. **a** Current flows through ions on the pore water (blue) and gas flows through the unsaturated pore space. **b** In unsaturated conditions, fractures create flow barriers for current and flow pathways for gas, causing a decrease in BEC and an increase in gas phase permeability. **c** In saturated conditions current flows through the pore water (blue), and **d** explosion-induced fractures provide low-tortuosity current flowpaths that increase BEC with respect to **c**

grains making up the solid fraction of the host rock are both electrically non-conductive and impermeable, so that both current and gas flows primarily

through the pore spaces between the mineral grains. Current flow is dominated by the drift of ions within the pore water, shown in blue in Fig. 3. Gas flows

predominantly through the unsaturated pore space, shown by the green arrows in Fig. 3. In unsaturated media (Fig. 3a) current flows through the water films coating the mineral grains, and therefore BEC is positively correlated with the pore water content (porosity and saturation) and pore fluid conductivity, and negatively correlated with the tortuosity of the current flow paths (Archie, 1944). Conversely, gas flows through the unsaturated pore space. Gas phase permeability is positively correlated with the unsaturated pore volume, and negatively correlated with the tortuosity of gas flow pathways. When an unsaturated solid matrix is fractured by an underground explosion as shown in Fig. 3B, the fracture tends to disconnect current flow pathways and produce a barrier to current flow, resulting in a decrease in BEC with respect to pre-explosion conditions. The same fracture provides a low-tortuosity gas flow pathway, resulting in an increase in gas phase permeability relative to pre-explosion conditions. Therefore, in an unsaturated system, a decrease in BEC from pre-detonation conditions is diagnostic of rock fracturing/damage and a corresponding increase in gas phase permeability.

In a fully saturated system explosion-induced fractures create low-tortuosity flowpaths for current flow as illustrated in Fig. 3c and d, causing an increase in BEC with respect to pre-detonation conditions. As noted above, protection of the GZ wellhead required that the GZ borehole be filled with water prior to detonation of each explosive experiment. This resulted in confounding variations in water content within the system that complicated interpretations of changes in BEC in terms of rock damage. As a result, we conducted time lapse ERT imaging under saturated conditions so that increases in BEC from pre-detonation conditions were uniquely diagnostic of rock damage. The same regions of increased BEC (e.g., damaged rock) are expected to exhibit increased gas phase permeability when the rock is desaturated (Fig. 3b and d).

2.8. Imaging Sequence

The general imaging sequence for each explosion is shown in Fig. 4. Prior to explosive Experiment 1, a static ERT survey was conducted to establish native

BEC conditions (Fig. 4A). Crosshole seismic velocity data were also collected as described in Sect. 2.5. Prior to each explosion, GZ was filled with water and maintained full for several hours to saturate the testbed (particularly fractures connected to GZ, Fig. 4B). Next the explosive package was lowered into position in GZ and detonated (Fig. 4C). After detonation, the testbed was left for several weeks to reach a new steady state. During this time water drains from the testbed (Fig. 4D). Next, after explosive Experiment 2 only, a heated air injection test was conducted as described in Sect. 2.4 (Fig. 4E). Each test concluded by refilling GZ with water to saturate the testbed and conducting another ERT survey. The change in BEC from Fig. 4A to B is caused by an increase in saturation (i.e., fractures filling with water) and therefore illuminates zones of pre-existing fractures. Increases in BEC from Fig. 4B to F are caused by increases in saturated porosity caused by the explosion, and therefore illuminate damage zones caused by the explosion. Noting the step B for explosive Experiment 2 is equivalent to Step F for explosive Experiment 1, it was possible to assess the damage caused by each explosion individually, as well as the total damage in terms of changes in BEC. Note also the flowrate required to maintain a constant head in step 4F was larger than that required in step 4B due to the generation of new fluid flow pathways, particularly for a constant head level above the damage zone.

3. Seismic and ERT Data

3.1. Baseline Crosshole Seismic

Crosshole seismic data were collected with source spacings of 1 m in wellbore SE and receiver spacings of 0.25 m in wellbore NW (Fig. 1A). First arrivals were picked manually and uncertain arrivals were culled from the data set, resulting in 4304 arrival times in the inverted data set. The data were inverted in 3D to account for borehole deviations. Errors between observed and simulated travel times and are shown in Fig. 5 in terms of absolute error in milliseconds and percent error. The corresponding velocity image is presented and discussed in Sect. 3.

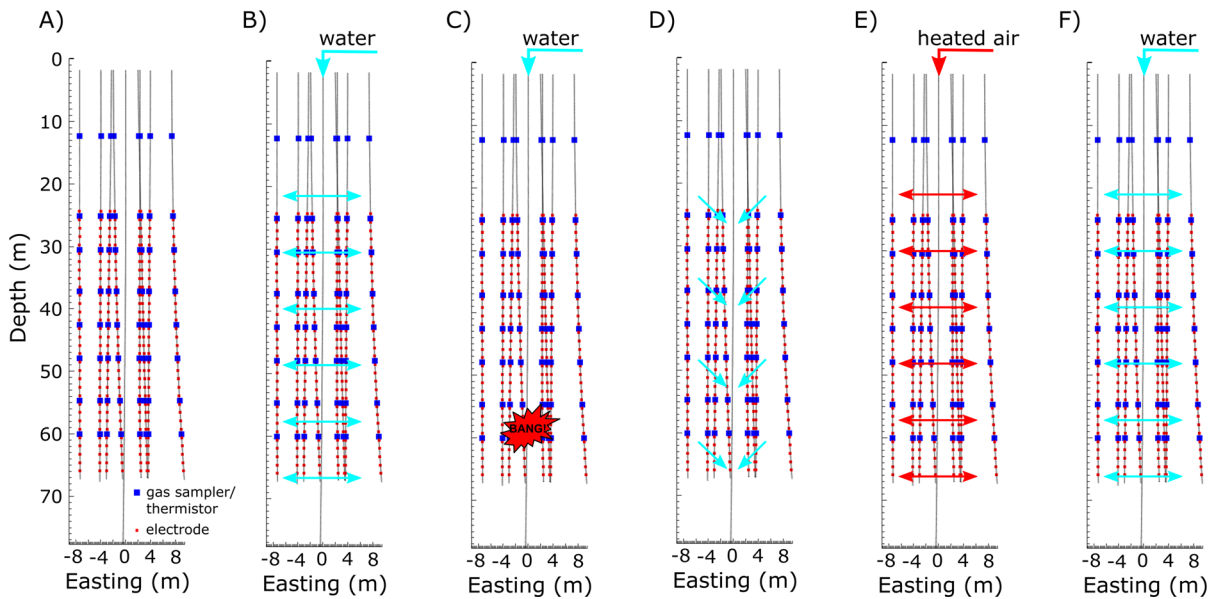


Figure 4

General testing sequence for each explosion. **A** Pre-testing ERT image to establish native conditions (prior to shot 1 only), **B** the testbed is saturated and imaged. The changes from step A illuminates pre-existing fracture zones. **C**) Shot is conducted. **D** Testbed is allowed to relax and drain for several weeks. **E** Time-lapse ERT imaging during heated air injection to image airflow pathways (after shot 2 only). **F** Testbed is re-saturated and imaged. The change in BEC from step B illuminates the damage zone

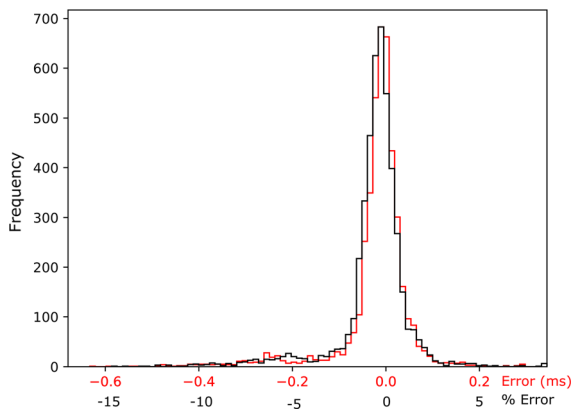


Figure 5

Absolute (black) and percent error (red) between observed and simulated seismic arrival time for the pre-test baseline crosshole seismic image

3.2. ERT Data

The ERT imaging zone extends from approximately 25–68 m below ground surface with a radius of approximately 8 m from the ground zero borehole. Equivalent 3D ERT surveys were collected for all time steps and included a mix of in-well and

crosswell dipole–dipole measurements with differing offsets between electrode pairs intended to provide optimal resolution within the ERT imaging zone. Twenty repeat surveys were collected prior to testing to establish noise conditions and filtering criteria for the time-lapse data. Data were culled if the standard deviation of the repeat measurements exceeded 10% of the observed value, or if transmitted currents were less than 10 mA. Of the 4010 measurements collected per survey, 561 were culled ($\sim 16\%$), leaving 3449 measurements per ERT survey. The same 3449 measurements were collected and processed for all of the results shown in Sect. 3.

Time-lapse ERT data were collected several days after each explosive experiment to monitor the recovery of the testbed. Time-lapse ERT data were also collected before, during, and after the GZ borehole was refilled to saturate the testbed, and during the heated gas injection experiment (see Fig. 4). Because the primary focus of this paper is on characterizing the rock damage caused by each explosive experiment, we do not show time-lapse ERT imaging results during post-explosion recovery

of the testbed or during testbed re-saturation (Fig. 4D and F respectively). However, Fig. 6 shows an example of a raw time-lapse ERT data series collected during explosive Experiment 2 for one of the 3449 measurements collected per survey. Figure 6, point A shows data collected in the pre-explosion saturated steady-state (Fig. 4B). Figure 6 points B, C and D show data collected during the post-shot recovery phase (Fig. 4D). The inset in Fig. 6 shows the location of the four electrodes used in the measurement and the corresponding approximate region of sensitivity with respect to the point of explosion. The explosion causes a large decrease in transfer resistance (increase in BEC) as water is driven into newly created fractures/damage. At point B, water is draining from the testbed and the water level is moving downward through the sensing volume causing a relatively rapid increase in transfer resistance (decrease in BEC) over a period of

approximately 3.5 h. At point C, the water level drops below the sensing volume. At point D water continues to percolate downward through sensing volume, causing a gradual increase in transfer resistance. Although the corresponding ERT images are not shown in this paper, Fig. 6 demonstrates the capability to monitor post-explosion dynamics using ERT imaging.

Appropriate data weighting is critical for effective time-lapse ERT imaging (Singha et al., 2015). Each ERT measurement was equally weighted for the time-lapse inversions and each ERT survey was fit to the same level of fidelity to ensure comparable images over time. Figure 7 shows a histogram of the percent error between observed and simulated ERT data for the pre-test baseline ERT image. Every subsequent data set was fit to approximately the same normal error distribution.

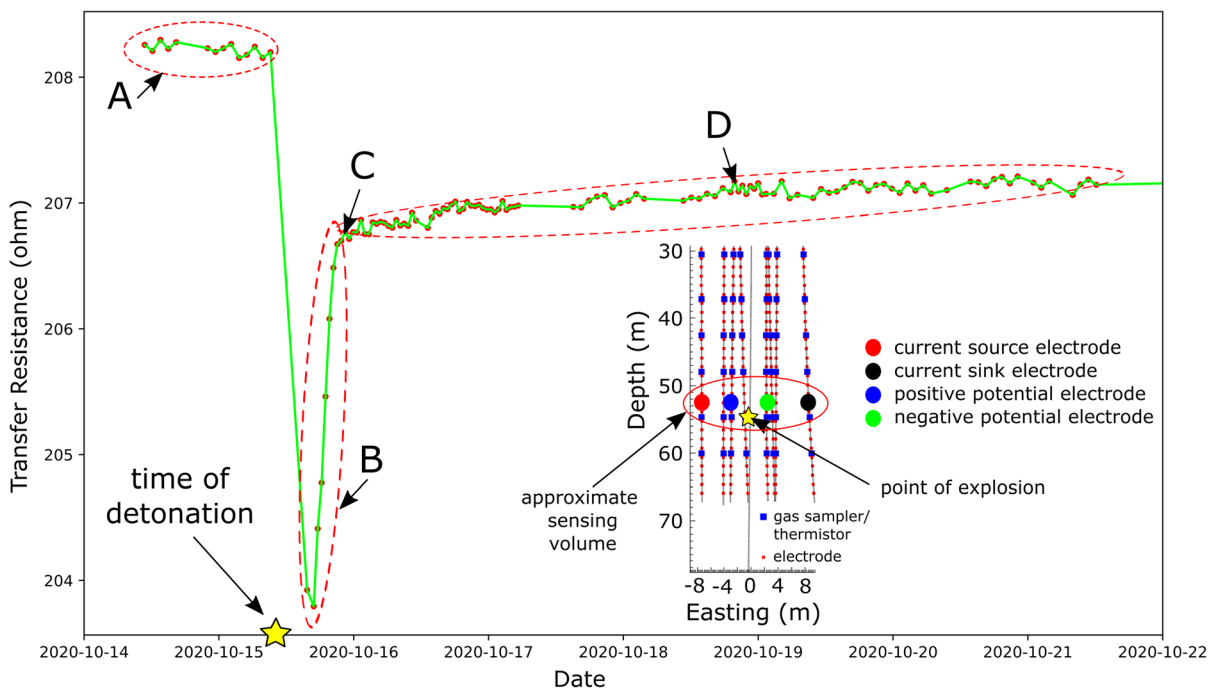


Figure 6

Time series for a single ERT measurement collected during Experiment #2. The inset shows the location of the explosion, the four electrodes used for the measurement, and the approximate sensing volume. Interval A shows the pre-detonation steady state condition with testbed saturated (Fig. 4B). Interval B shows the post shot time interval when the testbed is draining and the water level is dropping within the sensing volume. At point C, the water level drops below the sensing volume. During D the sensing volume continues to desaturate as water percolates downward through fractures

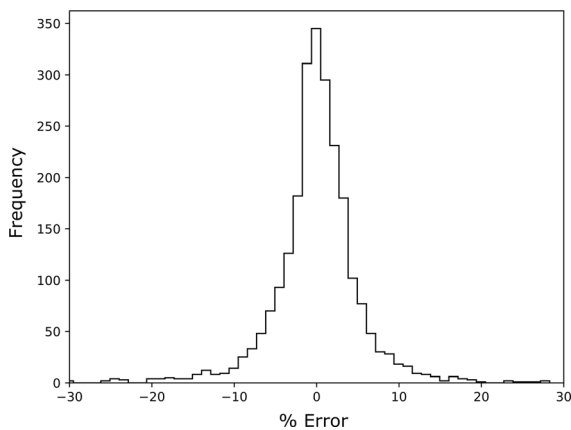


Figure 7

Distribution of percent error between the observed and simulated ERT data for the pre-test baseline ERT image. All subsequent data sets were fit to approximately the same error distribution

4. Results

4.1. Pre-experiment ERT and Crosshole Seismic Imaging

Figure 8 shows results of the ERT and seismic imaging characterization conducted prior to explosive Experiment 1 to characterize the native velocity structure of the testbed. Figure 8A shows the location of the 2D crosshole seismic image (blue line) and the ERT imaging volume (red circle) with respect to the GZ and each monitoring borehole. All subsequent ERT images are clipped at the red circle (8 m radius from GZ). Figure 8B shows two views of the 3D baseline ERT image of the testbed prior to saturation (i.e., Fig. 4A), revealing a layered rock fabric (in terms of BEC) dipping generally to the northwest. Figure 8C shows results of the time-lapse difference ERT image collected after the testbed was saturated (i.e., Fig. 4B) by injecting water into the GZ borehole. Here, changes in BEC from the baseline image (Fig. 8B) are shown as isosurfaces. Figure 8D shows the 2D crosshole seismic velocity image.

The seismic velocity image reveals a slow velocity zone (outlined in blue) presumably attributed to a less competent zone of naturally fractured rock that dips generally to the east. The anomalous increase in BEC (circled in red), which is caused by the presence of water introduced through GZ, occurs at the eastern downward dipping margin of the fracture zone. In tandem, the crosshole seismic and time-lapse ERT

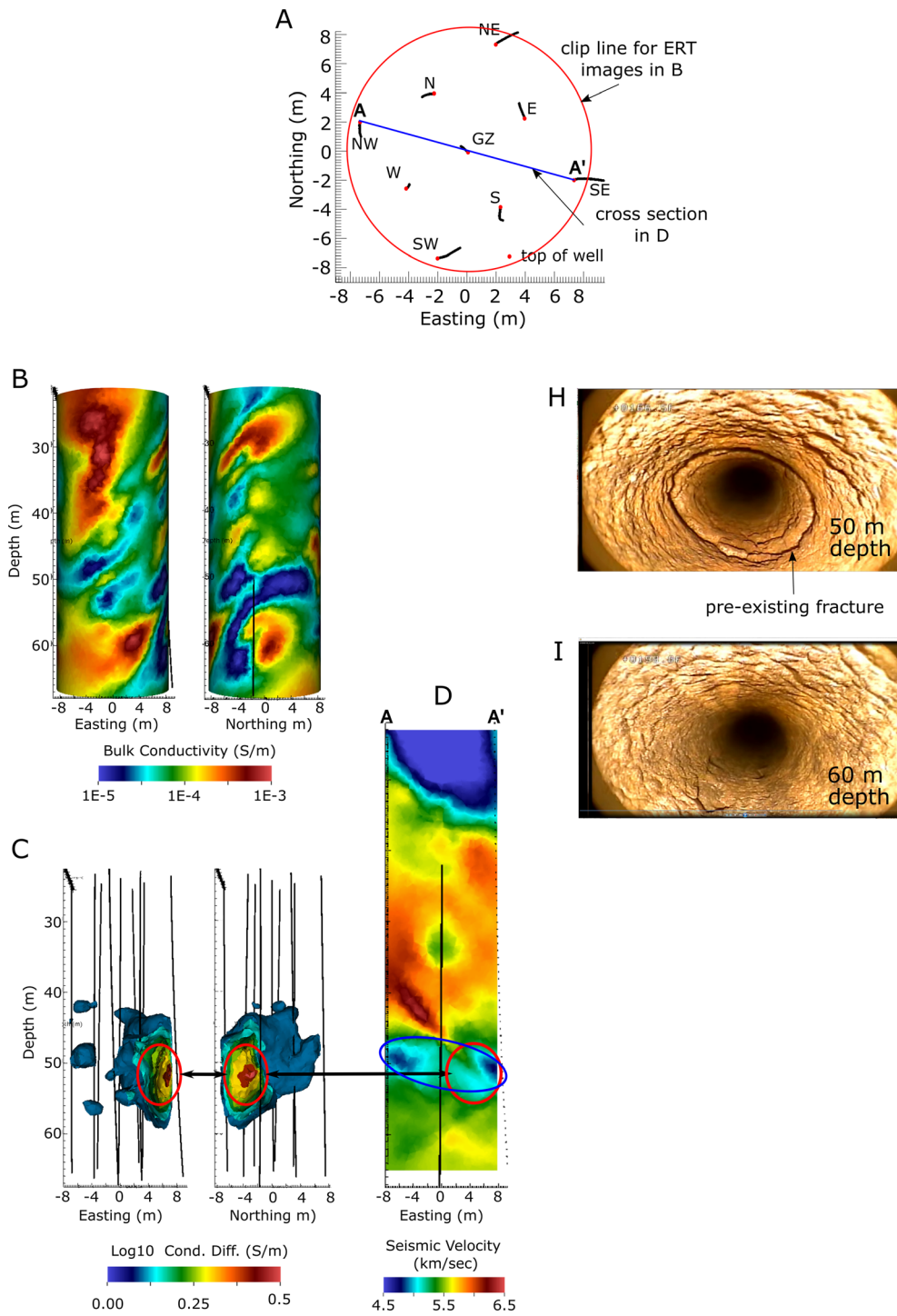
images provide corroborating evidence of a pre-existing natural fracture zone within the test bed. Namely, they show that water introduced into GZ during the saturation phase (Fig. 4B) entered the formation through the natural fracture zone and migrated down-dip and out of the ERT imaging volume. As will be shown, this pre-existing natural fracture zone had a dominating influence on rock damage patterns and gas flow paths for both Experiments 1 and 2. Figure 8H shows a borehole televiewer image at 50 m depth, verifying the location of a large fracture. Figure 8I shows a borehole televiewer image at 60 m depth (i.e. the explosive experiment 1 depth) for comparison.

4.2. 3D Damage Imaging

Figure 9 shows the pre-to-post explosion changes in saturated BEC (see Fig. 4F). Results are shown as 3D isosurfaces of the change in BEC from four different views as indicated in Fig. 9A. As described in Sect. 2, increases in BEC are diagnostic of increases in water filled fractures, or damage, caused by each explosion. Although ERT is incapable of resolving fracture apertures, regions of increased BEC outline the damage zones, with the magnitude of the increase being correlated to the magnitude of damage (i.e., the increase in fracture volume). Figure 9B–E shows the damage caused exclusively by explosive Experiment 1. Figure 9F–I show the damage caused exclusively by explosive Experiment 2, and Figure 9J–M show the total damage caused by both explosions. In View 1 and View 2, the blue and red outline correspond to the same outlines shown in Fig. 8C and D, respectively showing the locations of the low velocity zone and the water discharge zone observed in the baseline imaging.

For Experiment 1, the explosive was placed at 60 m depth in the GZ borehole. Figure 9B–E show that although there is some damage focused around the working point, most of the damage occurred approximately 10 m above the detonation depth within the natural fracture zone observed during baseline imaging (Fig. 8).

The explosive for Experiment 2 was denoted just beneath the primary damage zone generated by Experiment 1. As with Experiment 1, most of the



◀Figure 8

Results of pre-explosion ERT and crosshole seismic imaging. **A** Location of the seismic velocity section and ERT imaging volume with respect to ground zero (GZ) and monitoring boreholes. **B** Easting and Northing view of baseline ERT imaging results. **C** Isosurface views of the change in bulk electrical conductivity during water injection into GZ. **D** Baseline crosshole seismic velocity imaging results. **C** and **D** show that water introduced into GZ (outlined in red) migrated through an eastward-dipping natural fracture zone (outlined in blue). **H** Pre-explosion borehole televiewer image at 50 m depth showing pre-existing fracture. **I** Pre-explosion borehole televiewer image at 60 m depth (the detonation location of explosive experiment 1)

additional damage generated by Experiment 2 also appears to have been focused within the natural fracture zone. However, the magnitude of the increase in bulk conductivity for Experiment 2 is relatively muted in comparison. In both cases, most of the damage generated appears to be in the north-eastern margins of the natural fracture zone, and not local to the GZ borehole at the working point as might be expected.

4.3. Heated Gas Injection Imaging

Figure 10 shows several representative time-lapse ERT difference images collected during the heated gas injection experiment over 10 days of gas injection and 5 days of post inject recovery, oriented as in View 2 of Fig. 9A. Over the course of the injection, a negative BEC anomaly develops and grows along the upper margin of the damage zone. Later in time (e.g., days 7 and 8) positive BEC anomalies develop above and below the primary negative anomaly, centered around GZ. Post-injection, the positive anomalies vanish over time leaving only the negative anomaly at 5 days post injection.

These observations can be explained by the combined effect of evaporation and heating. As relatively dry, heated air is injected into GZ, it enters the formation primarily at the upper margin of the damage zone and migrates through the damage zone and out of the ERT imaging volume. As it migrates through the fracture zone, it evaporates water only until it reaches 100% humidity. As a result, evaporative drying occurs first near GZ and moves outward along the primary gas flowpath with time. The resulting decrease in water content causes the corresponding decrease in BEC shown in Fig. 10.

Due to the latent heat of vaporization, most of the energy in the heated air is taken up in evaporation as opposed to heating the host rock when evaporable water is present. When the rock becomes sufficiently dry, evaporation decreases and air temperature increases in the dried zone. As a result, the rock temperature increases, causing a corresponding increase in BEC. This process describes the positive BEC anomalies that develop a near GZ (i.e., the first regions to dry) above and below the evaporation zone. Post-injection, the rock cools causing positive BEC anomalies vanish. The negative BEC anomaly in the evaporated zone remains, marking the primary flowpath for gas.

5. Discussion

5.1. Rock Damage Mechanisms and Geologic Effects

In an underground chemical explosion, rock damage can be caused by both shock waves and by the fluid pressures generated during detonation and corresponding stresses exerted on the formation. For Experiments 1 and 2, damage from the shock wave was minimal as evidenced by the relatively intact GZ borehole left after each explosion. Damage was more likely caused by hydraulic fracturing because of the high fluid (gas and water) pressure pulse (more than 193 MPa) generated by each explosion. High pressure fluid could have accessed the natural fracture zone either through the GZ borehole or through new fracture pathways generated during the explosion. Close inspection of the ERT imaging results for Experiment 1 suggests it was the latter. For example, Fig. 9C (Experiment 1, View 2) shows a region of relatively high damage extending from the source point to the north and upward into the most damaged region of the natural fracture zone. Conversely, if the GZ borehole provided the primary conduit for fluid pressure into the natural fracture zone, we would expect more fracturing/damage near GZ within the natural fracture than is suggested by the ERT images. For example, the region of the natural fracture zone immediately surrounding GZ in Fig. 9B and E (Experiment 1, View 1 and View 4) shows relatively small damage in comparison to the region of the

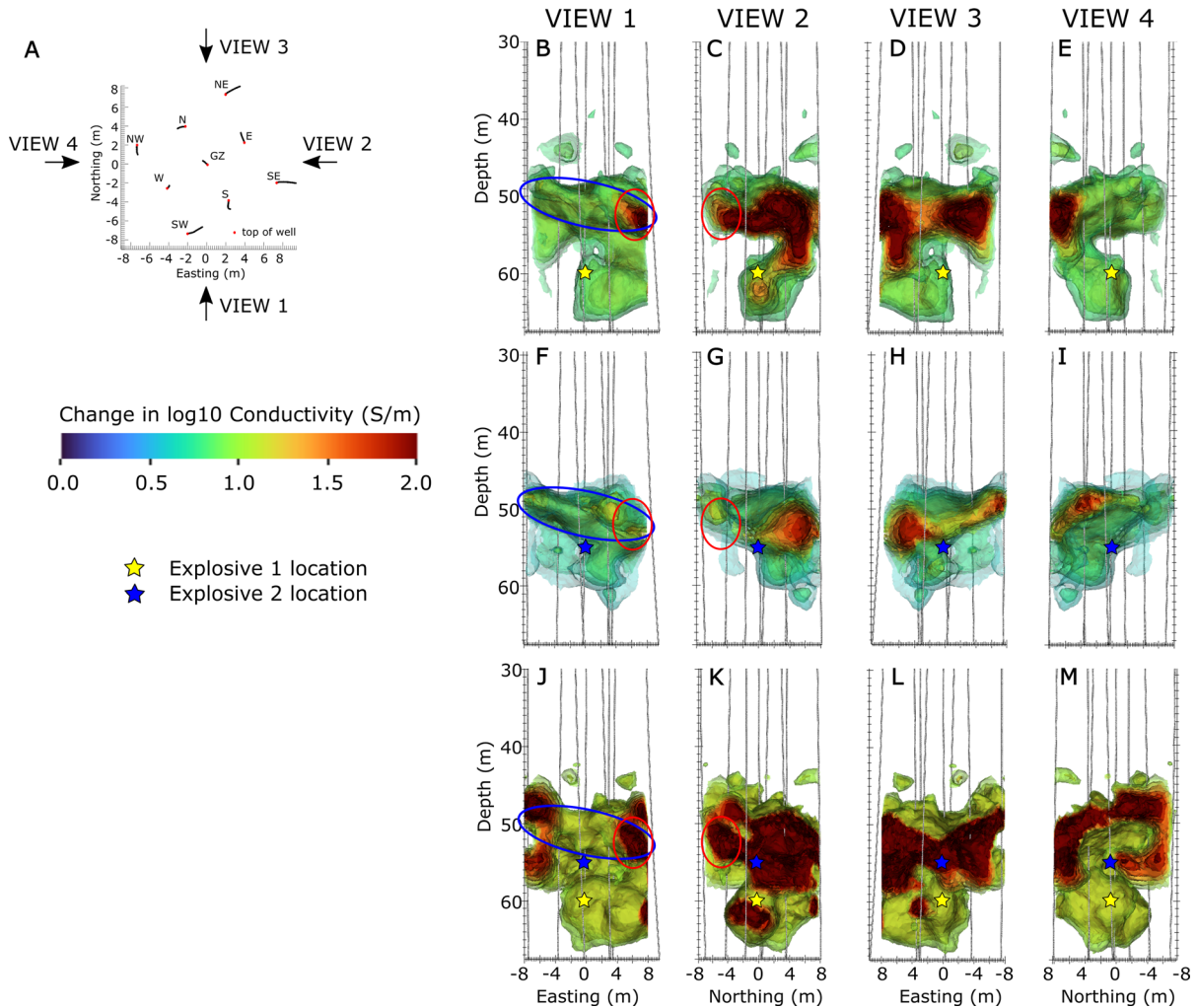


Figure 9

3D ERT pre-to-post explosion difference images expressed as isosurfaces of changes in BEC. **A** View orientations for **B–M**. **B–E** Damage zone resulting exclusively from explosive Experiment 1. **F–I** Damage zone resulting exclusively from explosive Experiment 2. **J–M** Total damage resulting from both experiments

natural fracture connected (by rock damage) to the source point shown in Fig. 9C. This suggests that the primary source of fluid pressure from the source point to the natural fracture zone was through fractures/damage generated by the explosion, and not through the GZ borehole.

For Experiment 2, the explosive was detonated just beneath the damage zone from Experiment 1. Consequently, fluid pressures generated by the explosion would have had a more direct path to previously fractured/damaged host rock. It is evident that the damage induced by Experiment 2 was not as

extensive as Experiment 1 in magnitude or extent. It is unclear whether this is the result of the slower denotation velocity and higher gas production in comparison to Experiment 1, or the result of the detonation being near previously damaged and therefore more compliant host rock, or both.

For both experiments, it is clear that the natural fracture zone identified in the baseline characterization had a governing influence on rock damage patterns. Although damage originating from each source point is evident, most of the damage occurred within the less competent existing fracture zone.

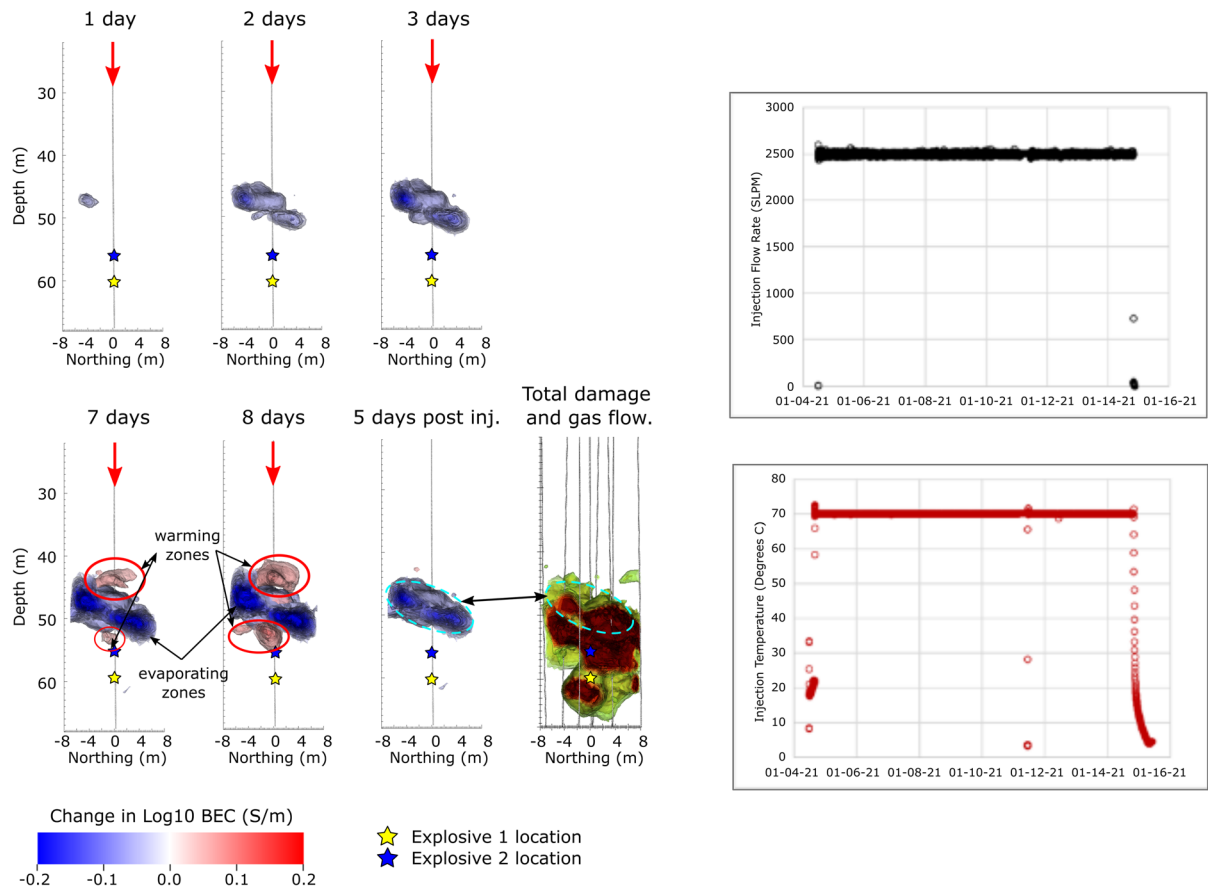


Figure 10

Time-lapse ERT imaging results during the heated gas injection experiment for 8 days of injection (red arrows), and for 5 days post-injection. For reference, the negative BEC anomaly (caused by water evaporation along the gas flow path) is super-imposed on the corresponding total damage image (Fig. 9K) by the light-blue dashed line. Injection flow rates and temperatures are included on the right

Namely, damage originating at the source point appears to have provided a transmissive pathway for high pressure fluids to enter and extend and/or expand the existing fractures. Furthermore, the damage zone is clearly non-symmetric in the horizontal direction, which is counter to simulations in homogeneous or layered media. Such behavior would have a significant impact on gas breakthrough times and locations at the surface in comparison to mechanically homogeneous or layered host rock. For example, high pressure gasses that intersect existing fracture zones could open/extend natural fractures and preferentially drive gases through them far from the source point and potentially in non-uniform directions, significantly impacting surface breakthrough times and locations in comparison to homogeneous host rock.

As noted in the Introduction, rock damage patterns can perturb seismic waves, and near-source mechanical heterogeneity could as well by similar reasoning.

5.2. Toward 'Dry' Explosion Damage Imaging

Experiments 1 and 2 focused on water injections into the GZ borehole for imaging the damage zone generated by each explosion, but other experiments may be conducted in a dry borehole, and the question remains of whether ERT is suitable for such cases. This paper demonstrates how time-lapse ERT can be used with heated air injections in unsaturated systems to image primary gas flow pathways from the source zone through the formation. Other works have shown how ERT monitoring can be used with reactive gas

tracers to illuminate gas flow pathways. For example, when NH_4 followed by CO_2 are injected into the subsurface, they partition into the pore water and participate in a reaction that increases pore water conductivity (Johnson et al., 2013), thereby illuminating gas flow pathways in terms of BEC. However, the question remains as to whether damage can be effectively imaged without introducing a contrast agent in unsaturated systems through the BEC change mechanism described in Fig. 3A and B and associated text.

To investigate, we conducted a laboratory scale imaging experiment on a tuff core sample. The core was instrumented with ERT electrodes, encased in epoxy, and imaged using 3D ERT before and after it was fractured using an embedded exploding bridge wire as shown in Fig. 11. The core was also imaged by X-ray tomography (XCT) for comparison to the ERT image. Imaging results are shown in Fig. 11.

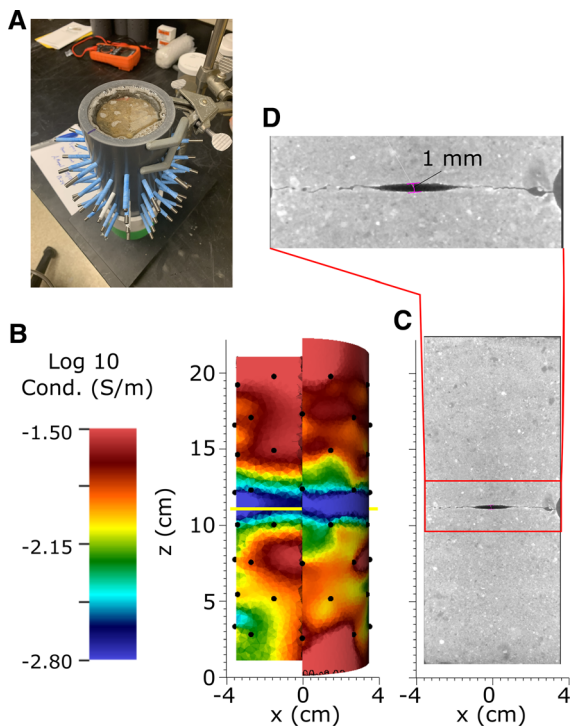


Figure 11

Results of core scale ERT imaging of a fracture zone without a contrast agent. **A** ERT imaging apparatus including tuff core instrumented with electrodes and embedded in epoxy. **B** Location of exploding bridge wire used to create the fracture (yellow) superimposed on a cut-out of the 3D ERT image. **C** and **D** XCT image of the fracture core

Figure 11A shows the test apparatus, including the core holder, electrodes, and core embedded in epoxy. Figure 11 B shows the location of the exploding bridge wire (yellow line) and the post-fracturing ERT image, and Fig. 11C and D show a cross section of the XCT. The fracture revealed by the XCT has an aperture of approximately 1 mm at its widest point (i.e., in the center where the exploding wire was located) and is approximately 0.1 mm elsewhere. Although the true dimensions of the fracture are not resolved in the ERT image, the fracture zone is correctly located and causes a decreased in bulk conductivity of nearly one order of magnitude. This large decrease in bulk conductivity for a 0.1–1.0 mm fracture aperture suggests damage imaging without a contrast agent in similar materials (i.e., tuff) is feasible.

6. Conclusions

We have demonstrated an emerging and robust approach for characterizing and monitoring the effects of underground chemical explosions using 3D and 4D ERT imaging. Specifically, we have demonstrated the use of ERT for imaging the pre-explosion structure of the host rock and the post-explosion damage and corresponding gas flow pathways. In conjunction with cross-hole seismic imaging, baseline imaging identified a pre-existing natural fracture zone. Post-explosion imaging revealed that the same natural fracture zone governed rock damage and gas flow patterns through the damage zone. These results point to the increased importance of geologic heterogeneity for understanding and modeling lower-yield UNE gas and seismic signals.

However, care must be taken when extending the observations from Experiments 1 and 2 to make specific inferences concerning the impacts of heterogeneity on gas transport and seismic signal behavior for larger underground chemical and nuclear explosions. For example, water saturation, host rock type, containment conditions and gas generation will generally differ significantly from the experiments in this work. The relative scale of geologic heterogeneities in comparison to explosive yield must also be considered. Nevertheless, the basic concepts

regarding the impacts of heterogeneous rock properties on damage and corresponding signal prediction demonstrated by Experiments 1 and 2 remain. Namely, natural fracture patterns and variations in rock strength on the scale of the damage zone are likely to play a significant role in gas breakthrough times, locations, and concentrations at the surface, and on seismic detection signal attributes. Furthermore, this work demonstrates an emerging capability for monitoring the effects of underground chemical explosions in 3D using static and time-lapse ERT imaging, particularly in the challenging near-source region.

Acknowledgements

The authors acknowledge important interdisciplinary collaboration with scientists and engineers from LANL, LLNL, MSTs, PNNL, and SNL. The authors gratefully acknowledge the assistance of the engineers and support staff at the Energetic Materials Research and Testing Center, Socorro NM, who performed the explosive operations for this test series and provide experimental support throughout.

Funding

This research was funded by the National Nuclear Security Administration, Defense Nuclear Nonproliferation Research and Development (NNSA DNN R&D).

Declarations

Conflict of interest The authors have no relevant financial or non-financial interests to disclose.

Ethical approval This paper describes objective technical results and analysis. Any subjective views or opinions that might be expressed in the paper do not necessarily represent the views of the U.S. Department of Energy or the United States Government. Sandia National Laboratories is a multi-mission laboratory managed and operated by National Technology & Engineering Solutions of Sandia, LLC, a wholly owned subsidiary of Honeywell International Inc., for the U.S. Department of Energy's National Nuclear Security Administration under contract DE-NA0003525.

Open Access This article is licensed under a Creative Commons Attribution 4.0 International License, which permits use, sharing, adaptation, distribution and reproduction in any medium or format, as long as you give appropriate credit to the original author(s) and the source, provide a link to the Creative Commons licence, and indicate if changes were made. The images or other third party material in this article are included in the article's Creative Commons licence, unless indicated otherwise in a credit line to the material. If material is not included in the article's Creative Commons licence and your intended use is not permitted by statutory regulation or exceeds the permitted use, you will need to obtain permission directly from the copyright holder. To view a copy of this licence, visit <http://creativecommons.org/licenses/by/4.0/>.

Publisher's Note Springer Nature remains neutral with regard to jurisdictional claims in published maps and institutional affiliations.

REFERENCES

- Angioni, T., Rechten, R. D., Cardimona, S. J., & Luna, R. (2003). Crosshole seismic tomography and borehole logging for engineering site characterization in Sikeston, MO, USA. *Tectonophysics*, 368(1–4), 119–137.
- Archie, G.E. (1942) The electrical resistivity log as an aid in determining some reservoir characteristics. *Transactions of the American Institute of Mining and Metallurgical Engineers* 146, 54–61.
- ASTM, D. (2007). 4428/D 4428M-07, Standard Test Methods for Crosshole Seismic Testing. *ASTM D*, 7400–08.
- Bauer, S. J. (2021). Laboratory measurements and field observations in support of blue canyon dome testing, SAND2021–6143. Sandia National Laboratories.
- Bowyer, S. M., Miley, H. S., Thompson, R. C., & Hubbard, C. W. (1997). Automated particulate sampler for Comprehensive Test Ban Treaty verification (the DOE radionuclide aerosol sampler/analyzer). *IEEE Transactions on Nuclear Science*, 44(3), 551–556. <https://doi.org/10.1109/23.603709>
- Bowyer, T. W., Schlosser, C., Abel, K. H., Auer, M., Hayes, J. C., Heimbigner, T. R., McIntyre, J. I., Panisko, M. E., Reeder, P. L., Satorius, H., Schulze, J., & Weiss, W. (2002). Detection and analysis of xenon isotopes for the comprehensive nuclear-test-ban treaty international monitoring system. *Journal of Environmental Radioactivity*, 59(2), 139–151. [https://doi.org/10.1016/S0265-931X\(01\)00042-X](https://doi.org/10.1016/S0265-931X(01)00042-X)
- Denny, M. D., & Johnson, L. R. (1991). The explosion seismic source function: Models and scaling laws reviewed. In S. R. Taylor, H. J. Patton, & P. G. Richards (Eds.), *Explosion source phenomenology, geophysical monograph series* (Vol. 65, pp. 1–24). AGU.
- Dietrich, P., & Tronicke, J. (2009). Integrated analysis and interpretation of cross-hole P- and S-wave tomograms: A case study. *Near Surface Geophysics*, 7(2), 101–109.
- Ekström, G., & Richards, P. G. (1994). Empirical measurements of tectonic moment release in nuclear explosions from teleseismic surface-waves and body-waves. *Geophysical Journal*

- International*, 117, 120–140. <https://doi.org/10.1111/j.1365-246X.1994.tb03307.x>
- Ford, S. R., & Walter, W. R. (2010). Aftershock characteristics as a means of discriminating explosions from earthquakes. *Bulletin of the Seismological Society of America*, 100(1), 364–376. <https://doi.org/10.1785/0120080349>
- Johnson, T. C., Versteeg, R. J., Ward, A., Day-Lewis, F. D., & Revil, A. (2010). Improved hydrogeophysical characterization and monitoring through parallel modeling and inversion of time-domain resistivity and induced-polarization data. *Geophysics*, 75(4), WA27–WA41.
- Johnson, T.C., et al. (2013) Determination of Water Saturation Using Gas Phase Partitioning Tracers and Time-Lapse Electrical Conductivity Measurements. *Vadose Zone Journal*, 12(2).
- Kalinowski, M. B., Axelsson, A., Bean, M., Blanchard, X., Bowyer, T. W., Brachet, G., Hebel, S., McIntyre, J. I., Peters, J., Pistner, C., Raith, M., Ringbom, A., Saey, P. R. J., Schlosser, C., Stocki, T. J., Taffary, T., & Kurt Ungar, R. (2010). Discrimination of nuclear explosions against civilian sources based on atmospheric xenon isotopic activity ratios. *Pure and Applied Geophysics*, 167(4–5), 517–539. <https://doi.org/10.1007/s00024-009-0032-1>
- Lowrey, J. D., Biegalski, S. R., Osborne, A. G., & Deinert, M. R. (2013). Subsurface mass transport affects the radioxenon signatures that are used to identify clandestine nuclear tests. *Geophysical Research Letters*, 40(1), 111–115. <https://doi.org/10.1029/2012GL053885>
- Luna, R., & Jádí, H. (2000). Determination of dynamic soil properties using geophysical methods. In: Proceedings of the first international conference on the application of geophysical and NDT methodologies to transportation facilities and infrastructure, St. Louis, (pp. 1–15).
- Singha, K., Day-Lewis, F. D., Johnson, T., & Slater, L. D. (2015). Advances in interpretation of subsurface processes with time-lapse electrical imaging. *Hydrological Processes*, 29(6), 1549–1576.
- Snelson, C. M., Abbott, R. E., Broome, S. T., Mellors, R. J., Patton, H. J., Sussman, A. J., Townsend, M., & Walter, W. R. (2013). Chemical explosion experiments to improve nuclear test monitoring. *Eos, Transactions American Geophysical Union*, 94(27), 237–239.
- Stroujkova, A. (2018). Rock damage and seismic radiation: A case study of the chemical explosions in New Hampshire. *Bulletin of the Seismological Society of America*, 108(6), 3598–3611.

(Received January 15, 2022, revised October 7, 2022, accepted October 10, 2022, Published online November 28, 2022)